

Driving Forces for Interfacial Fatigue Crack Growth by Piezoelectric Actuator

MING LIU^{1,3}, K. JIMMY HSIA^{1,*} AND JIAN-KU SHANG²

¹*Department of Theoretical and Applied Mechanics and* ²*Department of Materials Science and Engineering*
University of Illinois at Urbana-Champaign, Urbana, IL 61801, USA

³*Engineering Mechanics Corporation of Columbus, Columbus, OH 43221, USA*

ABSTRACT: A new experimental technique for accelerated fatigue testing has recently been developed (Du, T.B., Liu, M., Seghi, S., Hsia, K.J., Economy, J. and Shang, J.K. 2001. "Piezoelectric Actuation of Crack Growth along Polymer–Metal Interfaces in Adhesive Bonds," *Journal of Material Research*, 16(10):2885–2892). Using a piezoelectric actuator, cyclic loading can be applied at frequencies up to 20 kHz, several orders of magnitude higher than that achieved by a conventional mechanical cyclic loading technique. Moreover, the new technique using piezoelectric actuators directly addresses the debonding problem in piezoelectric multilayered smart structures. However, the threshold energy release rate for interfacial crack propagation, evaluated based on plane strain and linear piezoelectricity assumptions in (Du, T.B. 2001. "Durability of Polymer/Metal Interfaces under Cyclic Loading," PhD Thesis, University of Illinois at Urbana-Champaign, Urbana, IL, May), seems to be almost an order of magnitude lower than that measured by the conventional mechanical cyclic loading. In this article, we investigate the origin of such discrepancies, and find that the driving force provided by piezoelectric actuator is intrinsically three-dimensional in nature. To account for this effect, we develop both a plane strain model and a modified plane strain analytical model that takes into account the effects in the third dimension to evaluate the energy release rate. The results show that the plane strain solution underestimates the driving force. We also study the effect of nonlinear piezoelectricity on crack driving forces by performing detailed finite element simulations. The results show that the nonlinear piezoelectric effect is another important factor that contributes to the discrepancy between the results from the piezoelectric loading and that from the conventional mechanical loading.

Key Words: interfacial crack, piezoelectric bender, cyclic fatigue, finite element analysis, nonlinear piezoelectricity.

INTRODUCTION

PIEZOELECTRIC ceramics are widely used as mechanical actuators/sensors and in smart structures (Uchino, 1989, 1996). These structures are mostly bonded with adhesives, and are used under cyclic mechanical/electric loading. Interfacial fatigue crack propagation is often observed in these structures (Winzer et al., 1989; Furuta and Uchino, 1993; Kim and Jones, 1996). Therefore, interfacial fracture in adhesively bonded smart structures presents an important concern in multilayered devices. A better understanding of the coupled electromechanical failure mechanisms becomes critical for successful applications of piezoelectric materials in engineering structures.

On the other hand, polymer–metal interfaces are very common in applications ranging from aerospace and automobile structures to electronic devices. These multilayered structures often experience fluctuating loading conditions and may fail because of debonding due to fatigue crack growth. In order to increase interface durability, understanding of the failure mechanisms is essential. In the past, fatigue tests have been typically performed using mechanical actuators. However, the cyclic loading frequency of mechanical actuation systems can rarely go beyond 100 Hz. Although certain ultrasonic fatigue techniques can apply loading up to 20 kHz (Mason, 1950), they are not applicable to interfacial fatigue crack growth testing due to the reflection of ultrasonic stress waves at the interface. Therefore, new accelerated techniques for testing of interfacial fatigue are required to shorten the testing time needed for high-cycle fatigue experiments. Furthermore, a new technique capable of ultrahigh-frequency loading is the

*Author to whom correspondence should be addressed.
E-mail: kjhsia@uiuc.edu

only way to conduct ultra high-cycle fatigue testing (10^9 cycles and greater).

Fatigue failure in adhesively bonded smart structures limits the durability of these structures. On the other hand, such a failure mode presents a possible method for high-frequency interfacial fatigue testing. Inspired by this observation, we developed a new interfacial fatigue testing technique for polymer–metal systems (Du et al., 2001). Using a piezoelectric actuator, we can apply cyclic loading at frequencies up to 20 kHz, several orders of magnitude higher than the conventional testing techniques.

Unfortunately, the driving forces evaluated based on plane strain conditions and linear piezoelectricity models appear to be almost an order of magnitude lower than the real loading at the crack tip (Du, 2001). The difference could be due to the inherent three-dimensional (3D) loading conditions and/or the non-linear piezoelectric effects at high electric fields. In this article, the above issues are investigated in detail and the difference in the driving forces is explained.

GOVERNING EQUATIONS

Most poled piezoelectric ceramics exhibit transversely isotropic elastic behavior with hexagonal symmetry (Pak, 1992). With x_3 as the poling direction and the x_1 – x_2 plane as the isotropic plane, the constitutive equations for such piezoelectric materials can be written as:

$$\begin{aligned}\boldsymbol{\sigma} &= \mathbf{C}^E \boldsymbol{\varepsilon} - \mathbf{e}^T \mathbf{E}, \\ \mathbf{D} &= \mathbf{e} \boldsymbol{\varepsilon} + \boldsymbol{\epsilon}^E \mathbf{E},\end{aligned}\quad (1)$$

where the superscript T stands for the transpose of a vector or a matrix and $\boldsymbol{\sigma} = \{\sigma_{11} \ \sigma_{22} \ \sigma_{33} \ \sigma_{32} \ \sigma_{31} \ \sigma_{12}\}^T$, $\boldsymbol{\varepsilon} = \{\varepsilon_{11} \ \varepsilon_{22} \ \varepsilon_{33} \ 2\varepsilon_{32} \ 2\varepsilon_{31} \ 2\varepsilon_{12}\}^T$, $\mathbf{D} = \{D_1 \ D_2 \ D_3\}^T$, and $\mathbf{E} = \{E_1 \ E_2 \ E_3\}^T$ are the stress, strain, electric displacement, and electric field vectors, respectively. \mathbf{C}^E , \mathbf{e} , and $\boldsymbol{\epsilon}^E$ denote the stiffness matrix measured at zero electric field, the piezoelectric stress constant matrix, and the dielectric constant matrix measured at zero strain, respectively. They can be written in the matrix form as:

$$\mathbf{C}^E = \left\{ \begin{array}{cccccc} C_{11}^E & C_{12}^E & C_{13}^E & 0 & 0 & 0 \\ C_{12}^E & C_{11}^E & C_{13}^E & 0 & 0 & 0 \\ C_{13}^E & C_{13}^E & C_{33}^E & 0 & 0 & 0 \\ 0 & 0 & 0 & C_{44}^E & 0 & 0 \\ 0 & 0 & 0 & 0 & C_{44}^E & 0 \\ 0 & 0 & 0 & 0 & 0 & \frac{1}{2}(C_{11}^E - C_{12}^E) \end{array} \right\}, \quad (1a)$$

$$\begin{aligned}\mathbf{e} &= \left\{ \begin{array}{cccccc} 0 & 0 & 0 & 0 & e_{15} & 0 \\ 0 & 0 & 0 & e_{15} & 0 & 0 \\ e_{31} & e_{31} & e_{33} & 0 & 0 & 0 \end{array} \right\}, \\ \boldsymbol{\epsilon}^E &= \left\{ \begin{array}{ccc} \epsilon_{11}^E & 0 & 0 \\ 0 & \epsilon_{11}^E & 0 \\ 0 & 0 & \epsilon_{33}^E \end{array} \right\}.\end{aligned}\quad (1b,c)$$

Inverting Equation (1), the constitutive equations can also be expressed as:

$$\begin{aligned}\boldsymbol{\varepsilon} &= \mathbf{S}^E \boldsymbol{\sigma} + \mathbf{d}^T \mathbf{E}, \\ \mathbf{D} &= \mathbf{d} \boldsymbol{\sigma} + \boldsymbol{\epsilon}^\sigma \mathbf{E},\end{aligned}\quad (2)$$

where \mathbf{S}^E , \mathbf{d} , and $\boldsymbol{\epsilon}^\sigma$ denote the compliance matrix measured at zero electric field, the piezoelectric strain constant matrix, and dielectric constant matrix measured at zero stress, respectively. They are related to \mathbf{C}^E , \mathbf{e} , and $\boldsymbol{\epsilon}^E$ as follows:

$$\mathbf{S}^E = (\mathbf{C}^E)^{-1}, \quad \mathbf{d} = \mathbf{e} \mathbf{S}^E, \quad \boldsymbol{\epsilon}^\sigma = \boldsymbol{\epsilon}^E + \mathbf{e} \mathbf{d}^T. \quad (3)$$

The nonzero components of the piezoelectric strain constant matrix \mathbf{d} are

$$\mathbf{d} = \left\{ \begin{array}{cccccc} 0 & 0 & 0 & 0 & d_{15} & 0 \\ 0 & 0 & 0 & d_{15} & 0 & 0 \\ d_{31} & d_{31} & d_{33} & 0 & 0 & 0 \end{array} \right\}^T. \quad (3a)$$

The strain–displacement and the electric field–electric potential relations can be written as:

$$\varepsilon_{jk} = \frac{1}{2} \left(\frac{\partial u_j}{\partial x_k} + \frac{\partial u_k}{\partial x_j} \right), \quad E_j = -\frac{\partial \varphi}{\partial x_j}, \quad (j, k = 1, 2, 3), \quad (4)$$

where u_j and φ are the displacement components and electric potential, respectively.

If there is no body force or body charge, the equilibrium and the charge conservation equations are given by:

$$\sigma_{j,k,k} = 0, \quad D_{j,j} = 0, \quad (j, k = 1, 2, 3). \quad (5)$$

STEADY-STATE CRACK PROPAGATION

In this article, an adhesive–aluminum interface is studied. Figure 1 shows a schematic drawing of the setup for accelerated fatigue testing (Du et al., 2001), where h_p , h_e , and h_a are the thickness of PZT, adhesive, and aluminum layer, respectively, w is the width of all layers, and a is the length of an edge crack, c and C are the half length of PZT actuator and aluminum substrate, respectively. The poling direction of the piezoelectric actuator is along the positive y -axis. An electric potential drop V is applied through electrodes on the top and bottom of the PZT actuator.

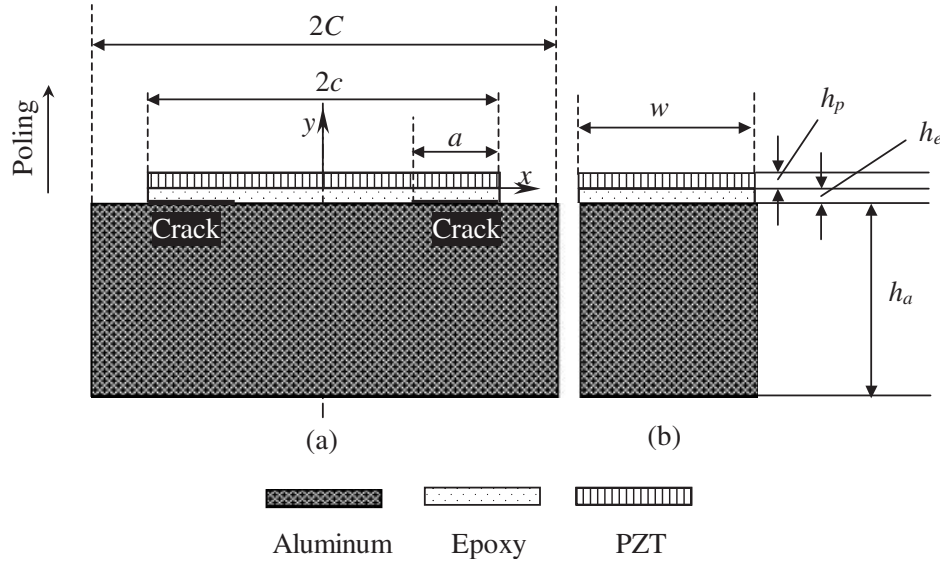


Figure 1. The accelerated fatigue testing system: (a) front view and (b) side view.

Table 1. Material properties.

PZT	$C_{11}^E = 13.8 \times 10^{10}$ Pa, $C_{33}^E = 12.9 \times 10^{10}$ Pa, $C_{12}^E = 8.83 \times 10^{10}$ Pa, $C_{13}^E = 9.39 \times 10^{10}$ Pa, $C_{44}^E = 2.45 \times 10^{10}$ Pa, $e_{31} = 1.02$ C/m ² , $e_{33} = 30.7$ C/m ² , $e_{15} = 14.0$ C/m ² ; $\epsilon_{11}^e = 151 \times 10^{-10}$ C/(Vm), $\epsilon_{33}^e = 130 \times 10^{-10}$ C/(Vm).
Adhesive	(Young's modulus) $E^e = 2.25$ GPa, (Poisson's ratio) $\nu^e = 0.4$.
Aluminum	(Young's modulus) $E^a = 62.1$ GPa, (Poisson's ratio) $\nu^a = 0.33$.

The finite element (FEM) software package ABAQUS (Version 5.8) is used to calculate the stresses near the crack tip. In the FEM calculations, plane strain condition is considered. The stress intensity factors are calculated from the stress distributions ahead of the crack tip. In our calculations, c is taken to be 22 mm, C and h_a are assumed to be 44 and 12.5 mm, respectively. We conducted a parametric study for different values of a , h_p , and h_e to evaluate their effects on crack driving forces. The material constants are given in Table 1. Because of the symmetric loading conditions and the symmetric geometry, only half the structure needs to be considered in the FEM model.

Figure 2 shows a particular mesh used in the calculation, where $h_p = 0.375$ mm, $h_e = 0.3$ mm, and $a = 6.6$ mm ($a/c = 0.3$). Figure 2(a) shows the entire FEM model of the multiplayer system, in which about 9000 four-node elements are used. Figure 2(b) shows the mesh near the crack tip. Piezoelectric elements that have an extra degree of freedom of electric potential are used for the PZT layer, and standard elastic elements are used for the adhesive and aluminum layer.

Since the crack is located between the adhesive layer and aluminum substrate, it has an oscillatory singularity at crack tip (Rice, 1988),

$$\begin{aligned}\sigma_{yy}(r, 0) &= \frac{1}{\sqrt{2\pi r}} \operatorname{Re}\{(K_I + iK_{II})r^{i\eta}\}, \\ \sigma_{xy}(r, 0) &= \frac{1}{\sqrt{2\pi r}} \operatorname{Im}\{(K_I + iK_{II})r^{i\eta}\}.\end{aligned}\quad (6)$$

We can define equivalent Mode I and Mode II stress intensity factors, K_I and K_{II} , respectively, as:

$$\begin{aligned}K_I(r) &= K_1 \cos(\eta \ln r) - K_2 \sin(\eta \ln r), \\ K_{II}(r) &= -\frac{1}{g_0} [K_1 \sin(\eta \ln r) + K_2 \cos(\eta \ln r)].\end{aligned}\quad (7)$$

It clearly shows that, in Equation (7), $K_I(r)$ and $K_{II}(r)$ for the interfacial crack are not constants. For nonzero η , they depend on the distance r from the crack tip. On the other hand, since the material mismatch constant η is usually very small (Rice, 1988; Liu and Hsia, 2003a), $K_I(r)$ and $K_{II}(r)$ are only weakly dependent on r . Thus over a fairly wide range of r (which could be the whole

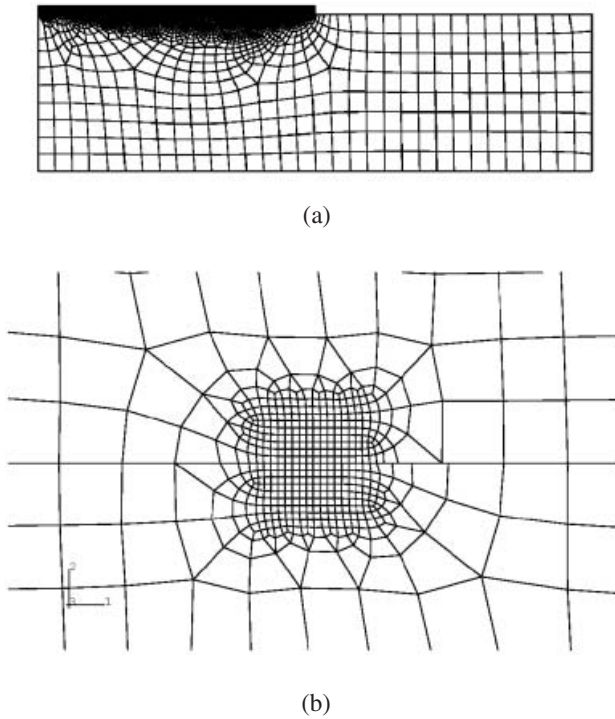


Figure 2. Finite element mesh: (a) overview and (b) local mesh near the crack tip.

K -dominant region), the values of $K_I(r)$ and $K_{II}(r)$ are approximately constant under a given far-field loading. Therefore, the stress intensity factors for interfacial cracks can still be calculated as:

$$K_I = \sqrt{2\pi r} \sigma_{yy}(r, 0)|_{r=\hat{r}}, \quad K_{II} = \sqrt{2\pi r} \sigma_{xy}(r, 0)|_{r=\hat{r}}, \quad (8)$$

where \hat{r} is an arbitrary position within the K -dominant region. As suggested by Rice (1988), we take \hat{r} as $0.02h_e$ ($0.02h_p$ when $h_e=0$) in the following calculations.

Due to mode coupling, the fracture toughness also depends on the mode mixity. Mode mixity is defined by the phase angle

$$\phi = \arctan\left(\frac{K_{II}}{K_I}\right)_{r=\hat{r}} \quad (9)$$

The FEM result in Figure 3 shows how K_I , K_{II} , and ϕ vary with crack length for $h_p=0.375$ mm, $h_e=0.3$ mm, and $E_0=V/h_p=8$ kV/cm. It is noted that, as the crack propagates, both K_I and K_{II} increase as the crack length increases for very small cracks (small a/c), and decrease rapidly when the crack is long ($a/c \sim 1$). For a wide range of crack length ($\sim 70\%$ of the total growth length), K_I and K_{II} are almost constant. Therefore, under cyclic electric potential loading, the crack propagation is expected to reach a steady state as the crack moves out of the edge zone. Such phenomenon has been found in some laminated structures (O'Brien, 1984; Suo, 1989; Thouless et al., 1989; Hutchinson and Suo, 1992). The dependence of mode mixity on crack length is similar to that of the stress intensity factors, and has an even wider

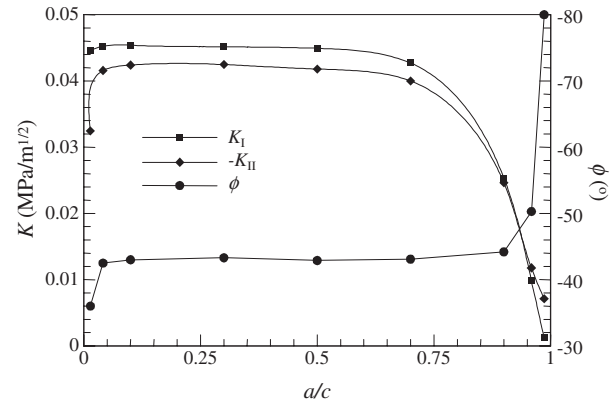


Figure 3. Stress intensity factors and mode mixity vs crack length.

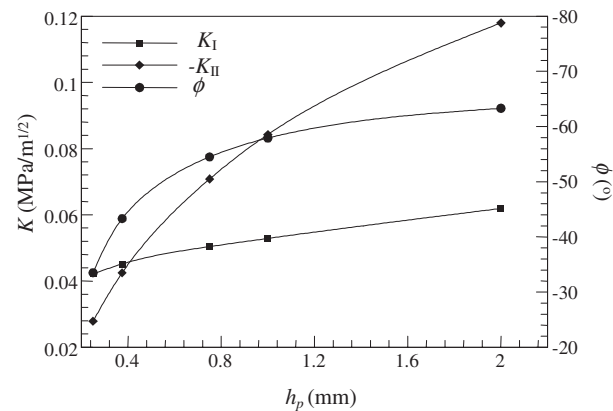


Figure 4. Stress intensity factors and mode mixity vs thickness of PZT actuator.

constant region. However, as the crack approaches the end, the phase angle increases sharply.

Figure 4 shows the effect of the thickness of PZT layer on the stress intensity factors and mode mixity. The calculation is conducted for $a/c=0.3$, $h_e=0.3$ mm, and $E_0=8$ kV/cm. The results show that both K_I and K_{II} increase as the PZT layer becomes thicker. In addition, a thicker PZT layer results in a larger phase angle.

Figure 5 shows the effect of the thickness of adhesive layer. As the thickness of adhesive layer increases, the Mode II stress intensity decreases, while the Mode I stress intensity increases. Normally, the fracture toughness is lower under Mode I loading than that under Mode II loading. Therefore, a thicker adhesive layer can reduce the apparent interface toughness. The results are for $a/c=0.3$, $E_0=8$ kV/cm, and $h_p=0.375$ mm.

ENERGY RELEASE RATE UNDER PLANE STRAIN ASSUMPTION

Basic Equations

Griffith energy release rate that provides the driving force for crack propagation in ferroelectric ceramics was

analyzed by Suo (1991). Under an applied mechanical force and electric voltage, the energy release rate, G , can be calculated as:

$$G = -\left(\frac{\partial \Pi}{\partial A}\right)_{F,V} = \left(\frac{\partial U}{\partial A}\right)_{F,V}, \quad (10)$$

where A is the crack area, F is the applied force and V the applied electric potential. Denoting Δ and Q as the energy conjugate displacement and electric charge, respectively, the functions $U(\Delta, Q, A)$ and $\Pi(F, V, A)$ are the total energy and potential energy, respectively.

When the steady-state crack propagation is achieved, the energy release rate is independent of the crack length. If the total energy per unit length (x -direction) per unit width (z -direction) of the specimen in the region far behind the crack tip is \bar{U}_b , and that far ahead of the crack tip is \bar{U}_a , the steady-state energy release rate can be easily calculated as:

$$G = \bar{U}_b - \bar{U}_a. \quad (11)$$

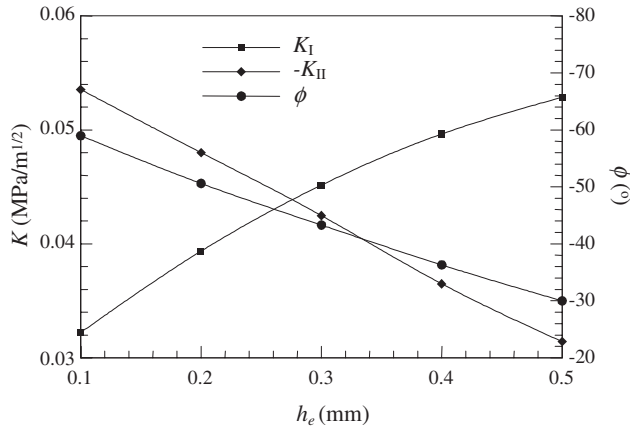


Figure 5. Stress intensity factors and mode mixity vs thickness of adhesive layer.

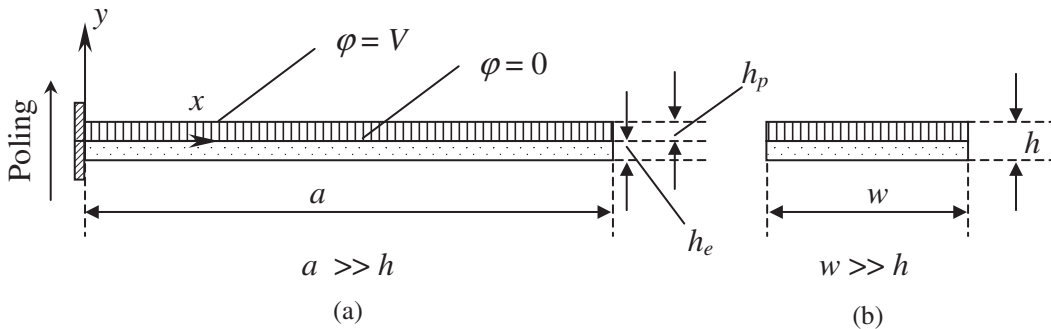


Figure 6. Piezoelectric bender: (a) front view and (b) side view.

The Region Far Ahead of Crack Tip

Since the thickness of the PZT and adhesive layers is significantly smaller than the aluminum substrate, the region far ahead of the crack tip can be simplified as an infinitely large PZT plate attached to an infinite substrate. Under such an assumption, the bending deformation generated by the applied electric potential on the PZT layer can be neglected. Therefore, the in-plane deformation of the entire multilayer structure should vanish. As a result, the deformation and electric potential in the PZT layer should be functions of y only, given as,

$$\begin{aligned} u_x^p(x, y, z) = u_z^p(x, y, z) = 0, \quad \phi^p(y=0) = 0, \\ u_y^p(x, y, z) = u_y^p(y), \quad \text{and} \quad \phi^p(y=h_p) = V, \quad (12) \\ \phi^p(x, y, z) = \phi^p(y), \quad u_y^p(y=0) = 0. \end{aligned}$$

substituting the above equations into the equilibrium equations, one can obtain the solution as:

$$\phi^p(y) = \frac{V}{h_p}y, \quad u_y^p(y) = -\frac{e_{33}}{C_{33}^E h_p}y. \quad (13)$$

The Region Far Behind of Crack Tip

When the crack is long enough ($a \gg h_p + h_e$), the region far behind the crack tip can be simplified as a piezoelectric bender (Xu et al., 1996; Wang et al., 1999) i.e., a bimaterial strip of PZT and adhesive layers as shown in Figure 6(a). Standard beam theory (Crawley and Anderson, 1990; Smits and Choi, 1991) incorporating piezoelectric coupling can be used to evaluate the stress and strain in the piezoelectric bender.

The standard beam solution is commonly obtained under plane stress conditions in the x - y plane. Figure 6(b) shows the cross section of a standard piezoelectric bender, and the height-to-width ratio is usually very small, $h/w \ll 1$ (Wang et al., 1999). In our tests, $h/w < 0.05$ (Du, 2001; Du et al., 2001). Therefore, a plane

strain condition is more appropriate for a beam theory solution.

Since the applied electric potential is uniform along the x -direction, it follows that the stress, strain, electric field, and electric displacement should be uniform in the x -direction, and the x -component of the electric field is zero. Therefore, the displacement and electric potential in the PZT and elastic layer should have the form

$$\begin{aligned} u_x^p(x, y) &= xt^p(y), & u_x^e(x, y) &= xt^e(y), \\ u_y^p(x, y) &= f^p(y) + g^p(x) & u_y^e(x, y) &= f^e(y) + g^e(x), \\ \varphi^p(x, y) &= \varphi^p(y), & \varphi^e(x, y) &= 0, \end{aligned} \quad (14)$$

where the superscripts p and e stand for quantities in PZT and adhesive materials, respectively. Under the plane strain condition, $u_z^p = u_z^e = 0$. The functions $t(y)$, $f(y)$, $\varphi(y)$, and $g(x)$ are functions of y or x to be determined by the governing equations and boundary conditions. The boundary conditions are given as:

$$\begin{aligned} \sigma_{xy}^p(y = h_p) &= \sigma_{xy}^e(y = h_p) = 0, & \sigma_{xy}^e(y = -h_e) &= 0, \\ \sigma_{yy}^e(y = -h_e) &= 0, & u_x^p(x = y = 0) &= u_x^e(x = y = 0) \\ &= u_y^p(x = y = 0) &= u_y^e(x = y = 0) &= 0, \\ u_x^p(y = 0) &= u_x^e(y = 0), & u_y^p(y = 0) &= u_y^e(y = 0), \\ \varphi^p(y = 0) &= 0, & \varphi^p(y = h_p) &= V, \end{aligned} \quad (15)$$

$$\begin{aligned} F_x &= \int_{-h_e}^0 \sigma_{xx}^e dy + \int_0^{h_p} \sigma_{xx}^p dy = 0, \\ M_z &= \int_{-h_e}^0 \sigma_{xx}^e y dy + \int_0^{h_p} \sigma_{xx}^p y dy = 0, \end{aligned}$$

where F_x and M_z are the total force along the x -direction and bending moment along z -axis on any cross-sectional area, respectively, and V is the applied potential on the top surface.

Substituting Equation (14) into Equations (2)–(4), and making use of the boundary conditions in Equation (15), we can derive the solution as:

$$\begin{aligned} u_x^p(x, y) &= x(a_0 y + a_1), & u_x^e &= x(a_0 y + a_1), \\ u_y^p(x) &= -\frac{a_0}{2} x^2 + \frac{\alpha}{2} a_0 y^2 + a_2 y, \\ u_y^e &= -\frac{a_0}{2} x^2 - \frac{C_{12} a_0}{C_{11} 2} y^2 - \frac{C_{12}}{C_{11}} a_1 y, \\ \varphi^p(y) &= \frac{\beta}{2} a_0 y^2 - \frac{1}{e_{33}} (C_{33}^E a_2 + C_{32}^E a_1) y, \end{aligned} \quad (16)$$

where

$$\alpha = -\frac{e_{32} + (\epsilon_{33}^e C_{32}^E / e_{33})}{e_{33} + (\epsilon_{33}^e C_{33}^E / e_{33})}, \quad \beta = -\frac{1}{e_{33}} (C_{33}^E \alpha + C_{32}^E). \quad (17)$$

The three coefficients a_0 , a_1 , and a_2 can be determined by the conditions

$$\begin{aligned} \frac{\beta}{2} h_p^2 a_0 - \frac{C_{32}^E}{e_{33}} h_p a_1 - \frac{C_{33}^E}{e_{33}} h_p a_2 &= V, \\ F_x &= \frac{1}{2} \left[h_p^2 (C_{11}^E + C_{13}^E \alpha + e_{32} \beta) - h_e^2 \left(C_{11} - \frac{C_{12}^2}{C_{11}} \right) \right] a_0 \\ &+ \left[h_p \left(C_{11}^E - \frac{C_{13}^E e_{32}}{e_{33}} \right) + h_e \left(C_{11} - \frac{C_{12}^2}{C_{11}} \right) \right] a_1 \\ &+ \left[h_p \left(C_{13}^E - \frac{C_{33}^E e_{32}}{e_{33}} \right) \right] a_2 = 0, \\ M_x &= \frac{1}{3} \left[h_p^3 (C_{11}^E + C_{13}^E \alpha + e_{32} \beta) + h_e^3 \left(C_{11} - \frac{C_{12}^2}{C_{11}} \right) \right] a_0 \\ &+ \frac{1}{2} \left[h_p^2 \left(C_{11}^E - \frac{C_{13}^E e_{32}}{e_{33}} \right) - h_e^2 \left(C_{11} - \frac{C_{12}^2}{C_{11}} \right) \right] a_1 \\ &+ \frac{1}{2} h_p^2 \left(C_{13}^E - \frac{C_{33}^E e_{32}}{e_{33}} \right) a_2 = 0. \end{aligned} \quad (18)$$

In the above equations, C_{11} and C_{12} are the stiffness of the adhesive. Once the displacement and electric potential are found, the strain, stress, and electric field, etc., can be obtained from the constitutive equations.

Energy Release Rate under Plane Strain Assumption

The total energy \bar{U}_a and \bar{U}_b can be calculated as:

$$\bar{U}_a = \int_0^{h_p} U_0^p dy, \quad (19)$$

$$\bar{U}_b = \int_{-h_e}^0 U_0^e dy + \int_0^{h_p} U_0^p dy, \quad (20)$$

where U_0^p and U_0^e are the energy density in PZT and elastic materials, respectively,

$$U_0^p = \frac{1}{2} \sigma_{ij} \epsilon_{ij} + \frac{1}{2} E_i D_i, \quad U_0^e = \frac{1}{2} \sigma_{ij} \epsilon_{ij}, \quad (i, j = x, y, z) \quad (21)$$

The energy release rate can then be calculated using Equations (11), (13), (16)–(21). It should be noted that the energy release rate predicted by this model is independent of the properties of the substrate.

The results of the energy release rate evaluated with the plane strain beam theory are listed in Table 2 for six different cases. It is noted that the first three cases explore the effect of different specimen geometries, whereas the last three cases investigate the effect of material property variations.

Along with the analytical solution, Table 2 also shows results from numerical calculations using the finite element method as described in the section ‘‘Steady State Crack Propagation’’. To evaluate the energy release rate numerically, two different methods are

Table 2. Evaluated energy release rate for different geometries and materials properties.

	Geometry (mm)			Materials properties	Energy release rate (J/m ²)		
	h_p	h_e	a		Plane strain solution	Numerical solution	
						Crack closure	SIF approach
Case 1	0.375	0.3	6.6	as in Table 1	0.76	0.76	0.73
Case 2	0.25	0.3	6.6	as in Table 1	0.51	0.51	0.48
Case 3	0.375	0.1	6.6	as in Table 1	0.78	0.78	0.74
Case 4	0.375	0.3	6.6	Table 1, except $E^e = 22.5$ GPa	0.71	0.71	0.69
Case 5	0.375	0.3	6.6	Table 1, except $E^e = 0.225$ GPa	0.78	0.65	0.62
Case 6	0.375	0.3	6.6	Table 1, except $E^a = 621$ GPa	0.76	0.77	0.75

used. Once the stress and displacement distribution in the vicinity of the crack tip is obtained using the finite element method, the energy release rate can be calculated either by the crack closure method or by the relationship between energy release rate and stress intensity factors.

The crack closure energy is the energy needed to close the crack and can be calculated as (Irwin, 1960):

$$G = \lim_{\delta \rightarrow 0} \frac{1}{2\delta} \int_0^\delta \sigma_{\theta\theta}(r, 0) \Delta u_y(\delta - r, \pi) dr + \lim_{\delta \rightarrow 0} \frac{1}{2\delta} \int_0^\delta \sigma_{r\theta}(r, 0) \Delta u_x(\delta - r, \pi) dr, \quad (22)$$

where Δu_x and Δu_y are the relative displacements between the top and bottom crack surfaces along the x - and y -directions, respectively. In finite element analysis, the above formula can be simplified with a modified crack closure method (Rybicki and Kanninen, 1977; Jih and Sun, 1990; Park and Sun, 1995).

Other than the crack closure method, under plane strain conditions, the energy release rate can be calculated from the stress intensity factors (Malyshev and Salganik, 1965), as

$$G = \frac{1 - \beta^2}{2} \left(\frac{1}{E^e + E^a} \right) (K_I^2 + K_{II}^2), \quad (23)$$

$$\beta = \frac{1}{2} \frac{\mu^e(1 - 2\nu^a) - \mu^a(1 - 2\nu^e)}{\mu^e(1 - \nu^a) + \mu^a(1 - \nu^e)},$$

where μ^e and μ^a are the shear modulus of the adhesive and aluminum, respectively.

The results in Table 2 show that the analytical and numerical solutions agree with each other very well except for case 5, where the adhesive layer becomes too weak to provide sufficient load transfer between the PZT layer and the aluminum substrate. Therefore, the deformation of the PZT and adhesive layers can no longer be neglected. The numerical results also show that the stiffness of the aluminum substrate almost has no effect on the energy release rate, which is consistent with the assumption in the analytical model.

ENERGY RELEASE RATE BY CONSIDERING THE FINITE WIDTH EFFECT

It is noted that both the numerical results in the section ‘‘Steady-State Crack Propagation’’ and the analytical results in the section ‘‘Energy Release Rate under Plane Strain Assumption’’ are obtained under the plane strain assumption. Such a condition would be satisfied only if the component is very wide i.e., when $a/w \ll 1$. However, in many realistic structures with piezoelectric actuators such as those used in our experiments (Du et al., 2001), the PZT actuator is more like a plate. Therefore, the plane strain assumption is questionable since the structure is actually under bending in both the x - and z -directions. To take into account the bending in the out-of-plane direction (z -direction in Figure 1), plate theory should be used. We modified the solution in the above section by adding several terms to the displacement components. If the bending moments in the x - and z -directions are not coupled, the displacement and potential should have the form

$$\begin{aligned} u_x^p(x, y, z) &= xt^p(y) & u_x^e(x, y, z) &= xt^e(y) \\ u_z^p(x, y, z) &= zq^p(y) & u_z^e(x, y, z) &= zq^e(y) \\ u_y^p(x, y, z) &= f^p(y) + g^p(x) + k^p(z), & & \\ u_y^e(x, y, z) &= f^e(y) + g^e(x) + k^e(z), & & \\ \varphi^p(x, y, z) &= \varphi^p(y) & \varphi^e(x, y, z) &= 0 \end{aligned} \quad (24)$$

where $q(y)$ and $k(z)$ are unknown functions to be determined. We also need additional boundary conditions to take into account the out-of-plane bending effect,

$$\begin{aligned} \sigma_{yz}^p(y = h_p) &= 0, & \sigma_{yz}^e(y = -h_e) &= 0, \\ u_z^p(x = y = z = 0) &= u_z^e(x = y = z = 0) = 0, \\ u_z^p(y = 0) &= u_z^e(y = 0), \\ F_z &= \int_{-h_e}^0 \sigma_{zz}^e dy + \int_0^{h_p} \sigma_{zz}^p dy = 0, \\ M_z &= \int_{-h_e}^0 \sigma_{zz}^e y dy + \int_0^{h_p} \sigma_{zz}^p y dy = 0. \end{aligned} \quad (25)$$

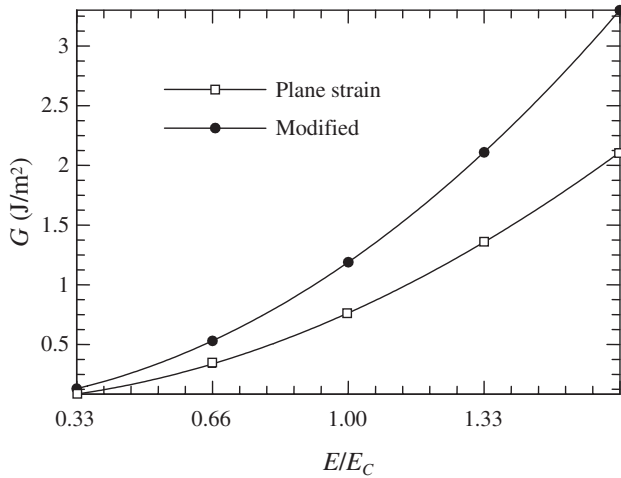


Figure 7. Energy release rate vs the electric field ($E_C = 8 \text{ kV/cm}$).

The solutions can then be obtained using the same procedures as those in the section “The Region for Behind of Crack Tip”.

Figure 7 shows the relationship between the energy release rate and the applied electric field. In evaluating the results, we take $h_p = 0.375 \text{ mm}$ and $h_e = 0.3 \text{ mm}$. The results indicate that under plane strain assumption, the energy release rate is underestimated. Due to the bending deformation in the out-of-plane direction, the actual energy release rate is larger than that from the plane strain solution given in the section “Energy Release Rate under Plain Strain Assumption”. The curve shown in Figure 7 follows a parabolic function of the electric potential, which can be fitted as:

$$G = G_0 \left(\frac{V}{h_p} \right)^2 \quad (26)$$

where $G_0 = 1.19 \times 10^{-12} \text{ J m}^2/\text{V}^2$ for plane strain solution, and $G_0 = 1.85 \times 10^{-12} \text{ J m}^2/\text{V}^2$ for the modified plane strain solution. It is noted that the value from the modified plane strain solution is about 1.6 times that from the plane strain solution.

Figures 8 and 9 show the energy release rate as a function of the thickness of the PZT or the adhesive layer, respectively. In Figure 8, the values $h_e = 0.3 \text{ mm}$ and $E_0 = 8 \text{ kV/cm}$ are used; and in Figure 9, $h_p = 0.375 \text{ mm}$ and $E_0 = 8 \text{ kV/cm}$ are considered. The result in Figure 8 shows that the energy release rate is almost proportional to the thickness of the PZT layer. Figure 9 shows that the energy release rate is nearly independent of the thickness of the adhesive layer, although the adhesive layer affects the mode mixity greatly (Figure 5).

PIEZOELECTRIC CONSTANTS AND DRIVING FORCES

Other than the geometry of the component and the loading amplitude, the properties of the material,

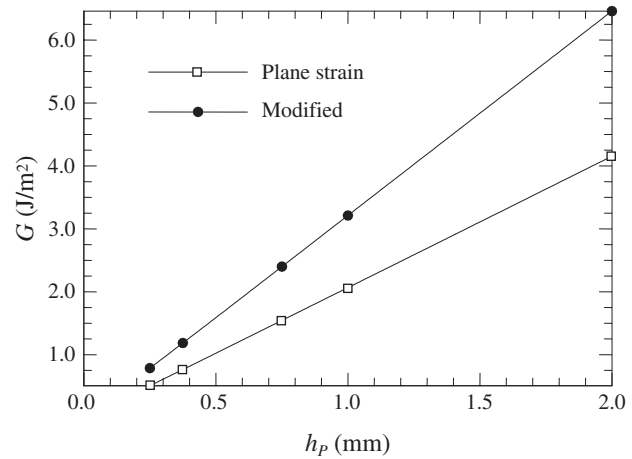


Figure 8. Energy release rate vs thickness of PZT actuator.

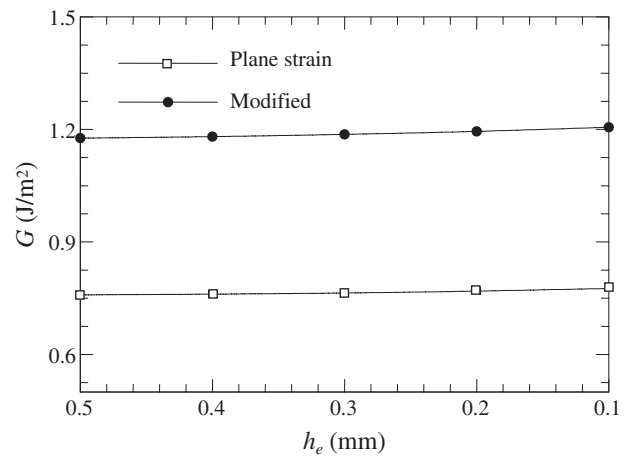


Figure 9. Energy release rate vs thickness of adhesive layer.

especially the piezoelectric constants have significant effects on the stress distribution. It should be pointed out that the piezoelectric constants vary profoundly among different piezoelectric materials. Therefore, by understanding the effects of the material constants on the stress intensity factors, one can choose the appropriate piezoelectric actuators for specific applications. Furthermore, the piezoelectric materials are inherently nonlinear. It is believed that the piezoelectric constants usually increase as the magnitude of the applied electric field increases (Kugel and Cross, 1998; Wang et al., 1998; Perrin et al., 2000; Hall, 2001). The nonlinearity is associated with non-180° domain switching and phase change (Liu and Hsia, 2003b; Liu et al., 2005). It is thus necessary to study the variation of the crack driving forces in terms of the material constants.

Figure 10 shows the effect of the piezoelectric constant, d_{31} , on the stress intensity factors and energy release rate for a layered structure shown in Figure 1. The results here are obtained using the finite element

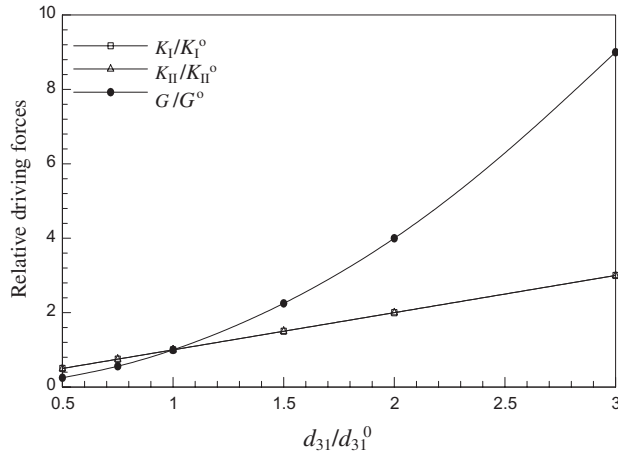


Figure 10. Crack driving forces vs piezoelectric constant d_{31} .

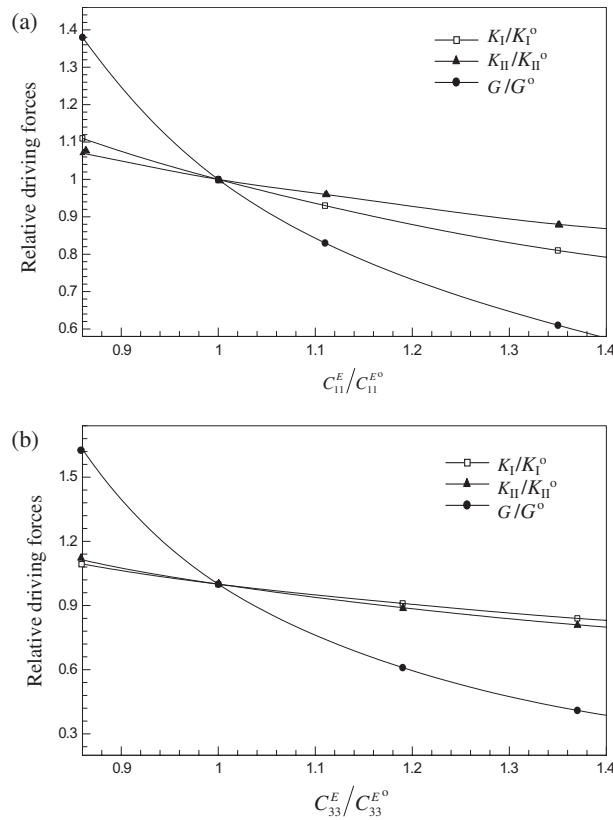


Figure 11. Crack driving forces vs stiffness constants: (a) C_{11}^E and (b) C_{33}^E .

method. The results are normalized by the corresponding values evaluated using the material constants listed in Table 1. Figure 10 shows that both K_I and K_{II} are proportional to d_{31} , and G is proportional to d_{31}^2 . Since the crack driving force is mainly generated by the electric field-induced strain within the plane of the PZT actuator, the driving force is almost independent of d_{33} . Figure 11 shows the effects of PZT's stiffness constants

on the stress intensity factors and energy release rate. It shows that, as the stiffness of the piezoelectric actuator increases, the crack driving force decreases. The above results are calculated for $h_e = 0$ mm (no adhesive layer), $h_p = 0.375$ mm, $a/c = 0.3$, and $E_0 = 8$ kV/cm; the d_{31}^0 , $C_{11}^{E^0}$, and $C_{33}^{E^0}$ are material constants from Table 1. The piezoelectric constants published are usually measured at very low electric field. However, at the electric field levels subjected by most piezoelectric actuators, the piezoelectric constants d_{31} and d_{33} could be as high as 1.5–2 times those of the published values (Kugel and Cross, 1998; Wang et al., 1998). Based on our calculations, such an increase in the piezoelectric constants will increase the energy release rate by a factor of 2.25–4.

Commercially available PZT materials can be divided into two categories. One is called hard PZT, such as PZT-4 and PZT-8, the other is soft PZT, such as PZT-5H and PZT-5A. A hard PZT material normally has higher stiffness and lower piezoelectric coefficients compared with a soft PZT. Therefore, a soft PZT material is preferred for applications as actuators. However, a soft PZT material has a larger hysteresis loop and generates more heat than a hard PZT material does under cyclic electric fields. As a result, a cooling system is often required for high frequency loading. Recently, new piezoelectric ceramics such as PMN-PT and PZN-PT have been developed. They have much larger piezoelectric coefficients than traditional PZT materials. Therefore, they could be good candidates for applications such as piezoelectric actuators providing cyclic mechanical loading if higher driving forces are needed.

In our experimental paper (Du et al., 2001), the energy release rate was calculated based on plane strain assumption and linear piezoelectricity model. It was found that, under piezoelectric loading, the driving force needed for fatigue crack growth was almost an order of magnitude lower than that under conventional mechanical cyclic loading. Our current results show that, by considering the finite width effects, the energy release rate increases by a factor of ~ 1.6 . The nonlinear piezoelectric effect can increase the energy release rate by a factor of 4. The combined effect of these factors can account for the discrepancy of the crack driving forces between piezoelectric loading and the mechanical loading results.

CONCLUSIONS

We have successfully developed a new accelerated fatigue testing technique for adhesive–metal interfaces using piezoelectric actuators, which is capable of applying loading at frequencies up to 20 kHz. Since this new technique employs a structure similar to many structures in smart devices, it can be used to directly

address the debonding problem in multilayered smart structures and devices.

Detailed finite element analyses of the crack driving forces have been conducted. The results show that this new technique can generate steady-state crack propagation. The crack driving force is almost constant during crack growth. The results also show that a thicker adhesive layer results in more Mode I stresses and therefore may give rise to lower apparent interface strength.

More importantly, we developed both plane strain and modified plane strain analytical solutions to the energy release rate. We found that the loading provided by the piezoelectric actuator is intrinsically 3D in nature. Therefore the solutions under plane strain condition underestimate the crack driving force.

Further, we found that the stress intensity factors are proportional to the piezoelectric constants, and the energy release rate is proportional to the square of the piezoelectric constants. Therefore, a soft PZT material that has smaller stiffness and larger piezoelectric properties can provide larger driving forces.

ACKNOWLEDGMENTS

The authors would like to acknowledge the support from the National Science Foundation under Grant No: CMS 98-72306.

REFERENCES

- Crawley, E.F. and Anderson, E.H. 1990. "Detailed Models of Piezoceramic Actuation of Beams," *Journal of Intelligent Materials, Systems, and Structures*, 1:4-25.
- Du, T.B. 2001. "Durability of Polymer/Metal Interfaces under Cyclic Loading," PhD Thesis, University of Illinois at Urbana-Champaign, Urbana, IL, May.
- Du, T.B., Liu, M., Seghi, S., Hsia, K.J., Economy, J. and Shang, J.K. 2001. "Piezoelectric Actuation of Crack Growth along Polymer-Metal Interfaces in Adhesive Bonds," *Journal of Material Research*, 16(10):2885-2892.
- Furuta, A. and Uchino, K. 1993. "Dynamic Observation of Crack Propagation in Piezoelectric Multilayer Ceramic Actuators," *Journal of the American Ceramic Society*, 76(6):1615-1617.
- Hall, D.A. 2001. "Review Nonlinearity in Piezoelectric Ceramics," *Journal of Materials Science*, 36(19):4575-4601.
- Hutchinson, J.W. and Suo, Z. 1992. "Mixed Mode Cracking in Layered Materials," *Advances in Applied Mechanics*, 29: 63-191.
- Irwin, G.R. 1960. "Fracture Mechanics," In: Goodier, J.N. and Hoff, N.J. (eds), *Structural Mechanics: Proceedings of the 1st Symposium on Naval Structural Mechanics*, 1958, Pergamon Press, New York, pp. 557-591.
- Jih, C.J. and Sun, C.T. 1990. "Evaluation of a Finite Element Based Crack-Closure Method for Calculating Static and Dynamic Strain Energy Release Rates," *Engineering Fracture Mechanics*, 37(2):313-322.
- Kim, S.J. and Jones, J.D. 1996. "Effects of Piezo-Actuator Delamination on the Performance of Active Noise and Vibration Control System," *Journal of Intelligent Material Systems and Structures*, 7(6):668-676.
- Kugel, V.D. and Cross, L.E. 1998. "Behavior of Soft Piezoelectric Ceramics under High Sinusoidal Electric Fields," *Journal of Applied Physics*, 84(5):2815-2830.
- Liu, M. and Hsia, K.J. 2003a. "Interfacial Cracks Between Piezoelectric and Elastic Materials under In-plane Electric Loading," *Journal of the Mechanics and Physics of Solids*, 51(5):921-944.
- Liu, M. and Hsia, K.J. 2003b. "Locking of Electric Field Induced Non-180° Domain Switching and Phase Transition in Ferroelectric Materials upon Cyclic Electric Fatigue," *Applied Physics Letters*, 83(19):3978-3980.
- Liu, M., Hsia, K.J. and Sardela, M. 2005. "In-situ X-Ray Diffraction Study of Electric Field Induced Domain Switching and Phase Transition in PZT-5H," *Journal of the American Ceramic Society*, 88(1):210-215.
- Malyshev, M. and Salganik, R.L. 1965. "The Strength of Adhesive Joints using the Theory of Cracks," *International Journal Fracture*, 5:114-128.
- Mason, W.P. 1950. *Piezoelectric Crystals and their Application in Ultrasonics*, Van Nostrand, New York.
- O'Brien, T.K. 1984. "Mixed-Mode Strain Energy Release Rate Effects on Edge Delamination of Composites," In: *Effects of Defects in Composite Materials, ASTM STP 836*, pp. 125-142, American Society for Testing and Materials, Philadelphia, Pennsylvania.
- Pak, Y.E. 1992. "Linear Electro-Elastic Fracture Mechanics of Piezoelectric Materials," *International Journal of Fracture*, 54(1): 79-100.
- Park, S.B. and Sun, C.T. 1995. "Fracture Criteria for Piezoelectric Ceramics," *Journal of the American Ceramic Society*, 78(6): 1475-1480.
- Perrin, V., Troccaz, M. and Gonnard, P. 2000. "Nonlinear Behavior of the Permittivity and of the Piezoelectric Strain Constant under High Electric Field Drive," *Journal of Electroceramics*, 4(1):189-194.
- Rice, J.R. 1988. "Elastic Fracture-Mechanics Concepts for Interfacial Cracks," *Journal of Applied Mechanics*, 55(1):98-103.
- Rybicki, E.F. and Kanninen, M.F. 1977. "A Finite Element Calculation of Stress Intensity Factors by a Modified Crack Closure Integral," *Engineering Fracture Mechanics*, 9:931-938.
- Smits, J.G. and Choi, W.-S. 1991. "The Constituent Equations of Piezoelectric Heterogeneous Bimorphs," *IEEE Transactions on Ultrasonics, Ferroelectrics, and Frequency Control*, 38(3): 256-270.
- Suo, Z. 1989. "Singularities Interacting with Interfaces and Cracks," *International Journal of Solids and Structure*, 25:1133-1142.
- Suo, Z. 1991. "Mechanics Concepts for Failure in Ferroelectric Ceramics," *Smart Structures and Materials*, AD-24/AMD-123:1-6.
- Thouless, M.D., Cao, H.C. and Mataga, P.A. 1989. "Delamination from Surface Cracks in Composite Materials," *Journal of Materials Sciences*, 24(4):1406-1412.
- Uchino, K. 1989. "Recent Topics of Ceramic Actuators: How to Develop New Ceramic Devices," *Ferroelectrics*, 91:281-292.
- Uchino, K. 1996. *Piezoelectric Actuator and Ultrasonic Motors*, Kluwer Academic, Boston.
- Wang, D. Fotinich, Y. and Carman, G.P. 1998. "Influence of Temperature on the Electromechanical and Fatigue Behavior of Piezoelectric Ceramics," *Journal of Applied Physics*, 83:5342-5450.
- Wang, Q.-M., Du, X.-H., Xu, B. and Cross, L.E. 1999. "Electromechanical Coupling and Output Efficiency of Piezoelectric Bending Actuators," *IEEE Transactions on Ultrasonics, Ferroelectrics, and Frequency Control*, 46(3):638-646.
- Winzer, S.R. Shankar, N. and Ritter, A. 1989. "Designing Cofired Multilayer Electrostrictive Actuators for Reliability," *Journal of the American Ceramic Society*, 72(12):2246-2257.
- Xu, B., Zhang, Q., Kugel, V.D., Wang, Q.-M. and Cross, L.E. 1996. "Optimization of Bimorph Based Double Amplifier Actuator under Quasistatic Situation," In: *Proceeding of the 10th IEEE International Symposium on Applications of Ferroelectrics*, East Brunswick, NJ, Vol. II, pp. 217-220.